Acta Materialia 161 (2018) 258–265

Contents lists available at ScienceDirect

Acta Materialia

journal homepage: www.elsevier.com/locate/actamat

Full length article

Good comprehensive performance of Laves phase $Hf_{1-x}Ta_xFe_2$ as negative thermal expansion materials

L.F. Li [a, b], P. Tong [a, b, *], Y.M. Zou [c], W. Tong [c], W.B. Jiang [a], Y. Jiang [a], X.K. Zhang [a, b], J.C. Lin [a, **], M. Wang [a], C. Yang [a, b], X.B. Zhu [a], W.H. Song [a], Y.P. Sun [a, c]

[a] Key Laboratory of Materials Physics, Institute of Solid State Physics, Chinese Academy of Sciences, Hefei, 230031, PR China
[b] University of Science and Technology of China, Hefei, 230026, PR China
[c] Anhui Province Key Laboratory of Condensed Matter Physics at Extreme Conditions, High Magnetic Field Laboratory, Chinese Academy of Sciences, Hefei, 230031, PR China

ARTICLE INFO

Article history:
Received 25 June 2018
Received in revised form
12 September 2018
Accepted 15 September 2018
Available online 19 September 2018

Keywords:
Laves phases
Negative thermal expansion
Electron spin resonance
Thermal conductivity
Young's modulus

ABSTRACT

Negative thermal expansion (NTE) materials can compensate for the normal positive thermal expansion (PTE) of most materials, and thus have great potential applications. Itinerant magnetic Laves phase compounds $Hf_{1-x}Ta_xFe_2$ with x ~0.16–0.22 exhibit an abrupt volume shrink as large as $\Delta V/V$ ~1% at the ferromagnetic (FM) to antiferromagnetic phase transition. Here we report that by reducing the Ta concentration the sharp volume change was gradually modified to a continuous one and moved to room temperature. NTE was optimized in $x = 0.13$, showing a linear NTE coefficient as large as −16.3 ppm/K over a broad window of 105 K (222 K - 327 K). As revealed by Electron Spin Resonance, the broadened NTE window is closely coupled with the asynchronous FM orderings of Fe moments at 6*h* and 2*a* Fe sites. In addition to good mechanical properties (i.e., Young's modulus, compressive strength and Vickers hardness), their thermal and electrical conductivities are superior to other metallic NTE materials, suggesting their wide applications as PTE compensators.

1. Introduction

Due to the inherent anharmonic atom vibrations, most solids expand upon heating, exhibiting positive thermal expansion (PTE) [1]. When the environment temperature is varied, the thermal expansion would lead to undesirable dimension change and thermal stress, which strongly affects the material performance and service life. Therefore, precisely controlling the coefficient of thermal expansion (CTE) of devices or components is strongly desired in rapidly developing modern industries [1,2]. The negative thermal expansion (NTE) materials, shrinking with increasing temperature, can be potentially used to compensate for PTE or to even realize zero thermal expansion by forming composite [3].

Besides a large NTE coefficient over a broad temperature range, many physical properties need to be considered for practical uses. Good mechanical properties, particularly a high Young's modulus, are especially demanded. In general, the bulk CTE of a composite is determined by averaging the components' CTEs weighted by their Young's moduli. In other words, the stiffer component has a greater impact on the bulk CTE [1]. For the purpose of designing compact and lightweight composites, a high bulk modulus of NTE materials is thus requested [4]. Thermal conductivity is another factor of crucial importance to the applications of NTE materials. A high thermal conductivity suggests that a sudden thermal shock can spread out quickly to achieve thermal homogeneity, which ensures high thermal stability and reliability of devices [5]. Combined excellent mechanical properties and thermal conductivity are particularly demanded for NTE materials employed in microelectronics [5], spatial applications [6] and cryogenic engineering [7].

By far the majority of NTE materials have open-framework crystal structures (e.g., ZrW_2O_8 [8], ScF_3 [9]), where soft phonons contribute to NTE. Due to the "soft" portion in the crystal structures, a low Young's modulus is inevitable. In some oxides, NTE can be triggered by charge transformation (e.g., $Bi_{1-x}La_xNiO_3$) [10] or by ferroelectric polarization ($Pb_{1-x}Bi_xVO_3$) [11]. Thermal conductivity is low due to the electron localization in those oxides. In itinerant electron magnets, the spontaneous volume magnetostriction

* Corresponding author. Key Laboratory of Materials Physics, Institute of Solid State Physics, Chinese Academy of Sciences, Hefei, 230031, PR China.
** Corresponding author.
E-mail addresses: tongpeng@issp.ac.cn (P. Tong), jclin@issp.ac.cn (J.C. Lin).

https://doi.org/10.1016/j.actamat.2018.09.029
1359-6454/

(SVM) [12], which links the spontaneous magnetization with lattice volume, can probably overcome the normal PTE due to anharmonic phonon contributions. A good example is the Invar alloys, whose low CTE or weak NTE was observed more than one century ago [12]. The itinerant electrons guarantee a relatively large thermal conductivity, while the non-soft-phonon NTE mechanism suggests a rather high Young's modulus. Therefore, itinerant electronic magnetism offers an opportunity to realize NTE phenomenon together with high thermal conductivity and mechanical properties [13–15].

The itinerant magnetic Laves phase $Hf_{1-x}Ta_xFe_2$ compounds with x ~0.16–0.22 exhibit an abrupt transition from the ferromagnetic (FM) ground state to antiferromagnetic (AFM) state when warming up [16–18]. Concomitant with the FM-AFM transition is a sharp volume contraction as large as ΔV/V ~1% [17]. Owing to the nature of first-order transition, the temperature window of this lattice contraction is very narrow, which restricts its practical applications as NTE materials. Here we report that by reducing the Ta concentration the abrupt volume change was successfully modified into continuous expansion and shifted to room temperature. For example, $x = 0.13$ compound shows NTE behavior with a linear CTE (α_L) = −16.3 ppm/K at 222 K - 327 K ($\Delta T = 105$ K). Analysis of bulk magnetic susceptibility and Electron Spin Resonance (ESR) spectra indicates the NTE is intimately entangled with the process of FM ordering. In $x = 0.13$ the Fe moments at the 2a and 6*h* sites evolve asynchronously at the paramagnetic (PM) to FM transition, while at the AFM-FM transition in $x = 0.2$ they act in concert. Moreover, those compounds have high thermal and electrical conductivities as well as good mechanical properties, beneficial to their potential applications.

2. Experiment

Polycrystalline samples of $Hf_{1-x}Ta_xFe_2$ ($0.1 \le x \le 0.25$) and $Hf_{0.9-y}Zr_yTa_{0.1}Fe_2$ ($0 \le y \le 0.2$) were prepared by arc melting the Hf rods (3N), Ta flakes (3N), Zr particles (3N) and Fe ingots (3N) with proper ratios in a cold copper crucible under purified argon atmosphere. To improve the homogeneity, the ingots were re-melted for extra five times and then annealed in evacuated quartz tubes at 1000 °C for 7 days.

Room temperature (RT) and temperature dependent X-ray diffractions (XRDs) were measured on a Philips X'pert PRO X-ray diffractometer with Cu K_α radiations. The scanning electron microscopy (SEM) measurements were carried out on a field-emission scanning electron microscope (FE-SEM, SU 8000, HITACHI). The elements mapping was measured on an Energy Dispersive X-ray Spectrometer (AZtec X-Max 80, Oxford) equipped on the SEM. Temperature dependent linear thermal expansion $\Delta L/L$ (using a strain gauge), thermal and electrical conductivities were measured on a Physical Property Measurement System (Quantum Design). The magnetization measurements were performed on a Superconducting Quantum Interference Device Magnetometer (Quantum Design). The temperature dependent ESR spectra were recorded using an X-band Bruker EMX plus 10/12 cw spectrometer operating at 9.4 GHz. ESR detects the power P absorbed by a sample from a transverse microwave magnetic field. The signal-to-noise ratio of the spectra was improved by recording the first derivative of P (dP/dH) with a lock-in technique.

Young's modulus was measured with a nano-indentation apparatus (MTS NANO Indenter® G200) at RT. Young's modulus and Poisson's ratio of the diamond were assumed as 1140 GPa and 0.07, respectively. The Poisson's ratio is set as 0.32 for $Hf_{1-x}Ta_xFe_2$ samples. Vickers microhardness measurement was carried out on a Vickers hardness tester 310HVS-5. For Young's modulus and Vickers hardness measurements, several test points up to ten were selected for each sample. The compression strength for $x = 0.13$ was obtained by a compression deformation test using Instron-5967 machine at RT.

3. Results and discussions

3.1. Negative thermal expansion

As shown in Figure S1 in the supplementary material, XRDs at RT for all $Hf_{1-x}Ta_xFe_2$ samples can be indexed with the space group $P6_3/mmc$ without any detectable diffractions from impurities. Fig. 1 shows a typical SEM image for $x = 0.13$ sample (those for $x = 0.1$ and 0.2 are shown in Figure S2 in the supplementary material). In the elements mapping (Fig. 1 and Figure S2 in the supplementary material), it is clear that the Hf, Ta and Fe elements are uniformly distributed at a scale of 100 μm for the three samples.

Fig. 2 shows the temperature dependent linear thermal expansion $\Delta L/L$ for $Hf_{1-x}Ta_xFe_2$. For parent compound $HfFe_2$, the α_L (~4 ppm/K) just below T_C (~600 K) is less than in the PM phase (α_L ~ 10 ppm/K), but NTE was not observed [19]. Upon doping with 10% Ta at Hf sites, NTE appears between 287 K and 356 K ($\Delta T = 69$ K) with $\alpha_L = -10.7$ ppm/K. With increasing Ta concentration to $x = 0.12$, the NTE window is expanded to $\Delta T = 87$ K (250 K - 337 K) and α_L is decreased to −14.4 ppm/K. As shown in Fig. 3, the temperature dependent XRDs between 110 K and 450 K indicates *a* (*b*) display NTE below T_C, while *c* shows PTE. Between 250 K and 340 K, the volumetric CTE for $x = 0.12$, α_V, is calculated to be −45.5 ppm/K ($\alpha_L \sim \alpha_V/3 = -15.2$ ppm/K), in good agreement with the $\Delta L/L$ presented in Fig. 2. As x increases to 0.13 (Fig. 2), NTE is further improved and α_L is ~ −16.3 ppm/K at 222 K - 327 K ($\Delta T = 105$ K), which is two times larger in magnitude than $Hf_{1-x}Nb_xFe_2$ (typically, $\alpha_L = -5 \sim -7$ ppm/K over 100 K) [20,21]. When $x > 0.14$ the NTE temperature window is narrowed instead of further expanded, though the magnitude of the lattice contraction is always increased with increasing x. For $x = 0.18$ and 0.2, $\Delta L/L$ displays a sharp jump of 0.28% and 0.35% at ~197 K and ~137 K, respectively, which is consistent with previous reports [17,18]. At $x = 0.25$, the abrupt jump of $\Delta L/L$ disappears, the sample exhibits a normal PTE behavior in the whole temperature range investigated.

In the nearly linear NTE range (277 K - 327 K, $\Delta T = 50$ K), the α_L of $x = 0.13$ reaches −29.3 ppm/K. This magnitude of NTE coefficient is three times that of the commercial ZrW_2O_8 material ($\alpha_L = -9$ ppm/K) [8], and even larger than the high-CTE metals, such as Al (23 ppm/K at RT). Such a high NTE performance is also comparable to those of reported metallic RT NTE materials. For instance, antiperovskite compound $Ga_{0.7}Ge_{0.3}N_{0.88}C_{0.12}Mn_3$ has a α_L of ~ −18 ppm/K at 197 K - 319 K ($\Delta T = 122$ K) [15], fine-sized $GaNMn_3$ displays NTE with $\alpha_L = -21.5$ ppm/K at 250 K - 360 K ($\Delta T = 110$ K) [22], and $LaFe_{10.5}Co_{1.0}Si_{1.5}$ has a α_L of −26.1 ppm/K between 240 K and 350 K ($\Delta T = 110$ K) [13].

For the purpose of wide applications, the prices of raw materials have to be taken into account. Hafnium is so chemically similar to zirconium that separating the two elements is extremely hard, resulting in a high price of high-pure hafnium. Impurities in Hf metal include mainly Zr. In order to test whether and how the Zr influences the NTE properties, we prepared the $Hf_{0.9-y}Zr_yTa_{0.1}Fe_2$ compounds. As shown in Fig. 4, the NTE behavior of $y = 0$ sample is preserved in the $y > 0$ samples. The absolute value of α_L is slightly increased with y, but the ΔT is significantly expanded to lower temperatures. For $y = 0.2$ (equivalently, the purity of Hf is about 77.8%), ΔT is as large as 112 K (240 K - 352 K). Consequently, it is economical and feasible to choose low-purity Hf for the synthesis of $Hf_{1-x}Ta_xFe_2$ NTE materials.

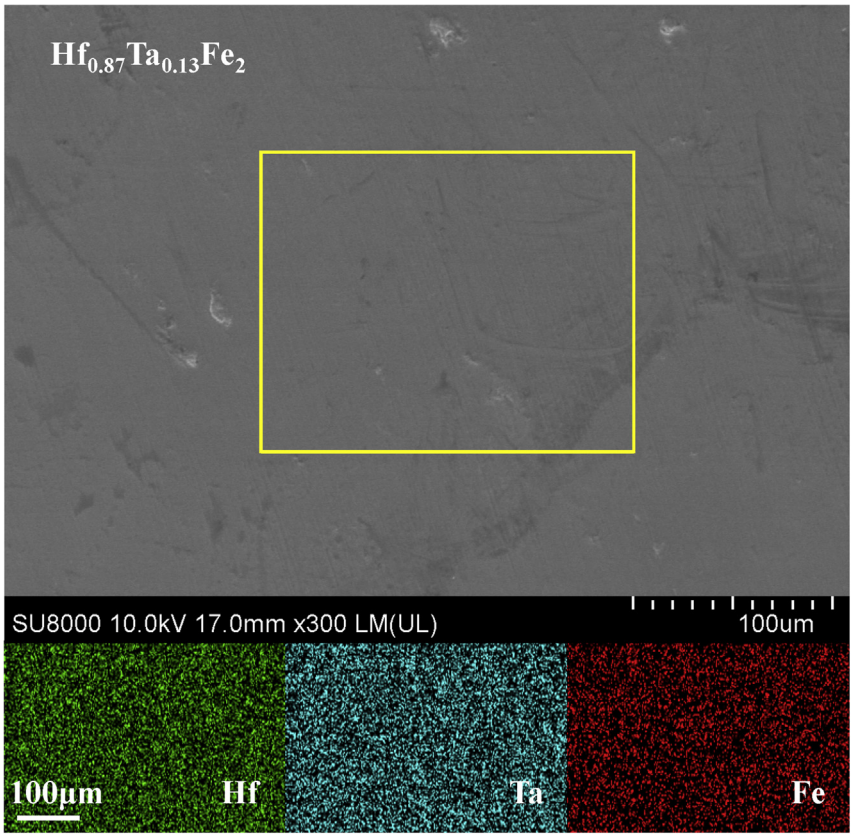

Fig. 1. SEM image (top) and elements mapping (bottom) of $Hf_{0.87}Ta_{0.13}Fe_2$ sample.

3.2. Spontaneous volume magnetostriction

Figure S3 (in the supplementary material) displays the temperature dependent magnetization M(T)s of $Hf_{1-x}Ta_xFe_2$ ($x = 0.1$, 0.13 and 0.2) measured at $H = 500$ Oe under zero-field-cooling mode. For $x = 0.1$ and 0.13, M(T) exhibits a FM to PM transition at $T_C \sim 341$ K and 307 K, respectively. While for $x = 0.2$, two transitions were observed when cooled from high temperatures. A PM to AFM transition happens at T_N ~350 K, followed by a sharp AFM to FM transition at ~145 K. The AFM-PM transition is also indicated by a broad kink at around 350 K in the $\Delta L/L$(T) curves for $0.16 \leq x \leq 0.2$ as shown in Fig. 2a. Fig. 5a and b shows the dM/dT and $d(\Delta L/L)/dT$ as a function of temperature for selected samples, respectively. The NTE window fairly coincides with the transition from PM (or AFM) to FM phase indicated by the valley of dM/dT. This confirms a strong coupling of the NTE behavior with the magnetism, which is often observed in itinerant magnets. We note that the $\Delta L/L$ curves were measured with descending temperature, while M(T) was collected with ascending temperature. So a thermal hysteresis between the minimum values of dM/dT and $d(\Delta L/L)/dT$ curves was observed. As shown in the inset of Fig. 5b, the hysteresis is reduced from 12 K for $x = 0.2$ to 4 K for $x = 0.13$ and finally to 2 K for $x = 0.1$. The tiny thermal hysteresis is in favor of practical applications.

In the scenario of SVM, the lattice volume change is governed by a certain magnetic order and its evolution with temperature. For example, in antiperovskite $Cu_{0.5}Ge_{0.5}NMn_3$ compound a gradual development of the Γ^{5g} AFM moment was observed, which covers a large temperature span where the lattice volume expands upon cooling [23]. For itinerant electron ferromagnets, the magnitude of SVM, ω_S ($\sim 3 \times \Delta L/L$), is related to the FM spontaneous magnetization (M_S) below T_C by the relation, $\omega_S = K \cdot M_S^2$, where K is the magnetoelastic coupling constant [19]. As shown in Fig. 2a, $x = 0.25$ compounds exhibits normal PTE without any signatures of NTE down to 20 K. So, the ω_S(T) for other compounds can be estimated by subtracting the $\Delta L/L$(T) of $x = 0.25$ from their curves. As shown in Figure S4 (in the supplementary material), below T_C the magnetization is almost saturated at 50 kOe. So the magnetization at 50 kOe (M_{50kOe}) gives a reasonable estimation of M_S. The square of M_{50kOe} (M_{50kOe}^2) and ω_S are plotted as a function of reduced temperature (T/T_C-1) in Fig. 5c and d for $x = 0.1$ and 0.13, respectively. Both M_{50kOe}^2 and ω_S display a similar temperature dependence below T_C, confirming that the SVM mechanism works for the NTE phenomena in $Hf_{1-x}Ta_xFe_2$. Unlike $x = 0.1$ and 0.13, the magnetization at 50 kOe for $x = 0.2$ is increased suddenly when cooled from the AFM to FM state (Figure S3 in the supplementary material). This abrupt growth of ferromagnetism accounts for the narrow NTE window (Fig. 2a) in terms of the SVM mechanism.

3.3. ESR study on the magnetic transitions

ESR is a powerful probe of local magnetism and is helpful for distinguishing the different magnetic orders and their evolutions with temperature [24,25]. Here ESR spectra for $x = 0.13$ and 0.2, showing different NTE behaviors, were measured and compared (Fig. 6). For clarity, the spectra are offset vertically and the spectra of $x = 0.13$ at some temperatures are divided by constant values (either 2, or 4 or 8). Original data without any treatments can be found in Figure S5 and Figure S6 in the supplementary material for $x = 0.13$ and 0.2, respectively. For both compounds, there is only one single resonance line at 500 K, which is well above the

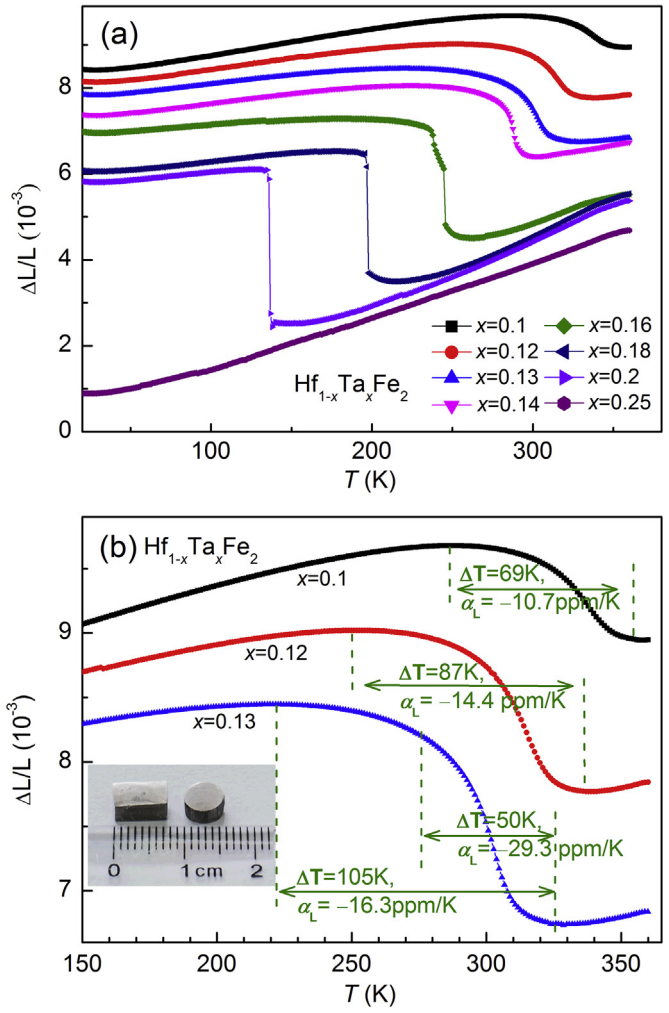

Fig. 2. (a) Linear thermal expansion $\Delta L/L$ (360 K) for $Hf_{1-x}Ta_xFe_2$ ($0.1 \le x \le 0.25$). (b) The enlarged plot of $\Delta L/L$ (360 K) curves of negative thermal expansion (NTE) range for $x = 0.1$, 0.12 and 0.13. Average linear coefficient of thermal expansion (α_L) and related temperature span (ΔT) of NTE are marked.

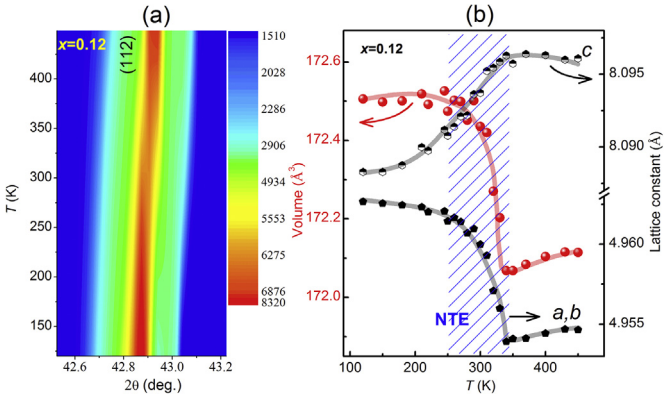

Fig. 3. (a) Contour plots of the (112) XRD profile intensity for $x = 0.12$ as a function of temperature. (b) The lattice constants (a, b, c) and unit cell volume as a function of temperature.

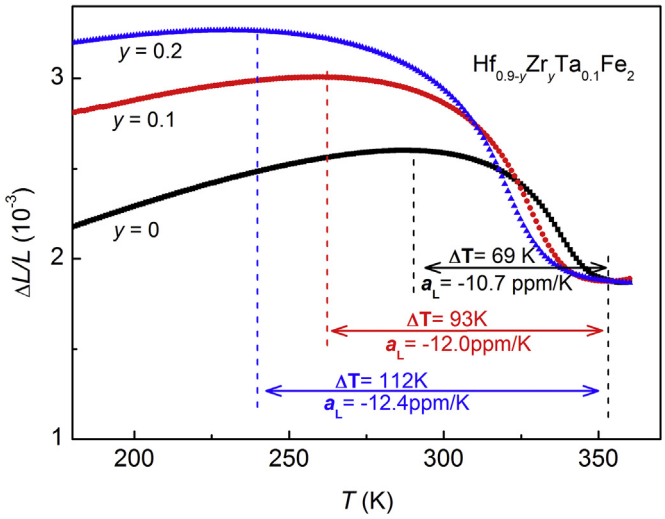

Fig. 4. Linear thermal expansion $\Delta L/L$ (360 K) for $Hf_{0.9-y}Zr_yTa_{0.1}Fe_2$ ($y = 0$, 0.1 and 0.2). Average linear coefficient of thermal expansion (α_L) and related temperature span (ΔT) of negative thermal expansion are marked.

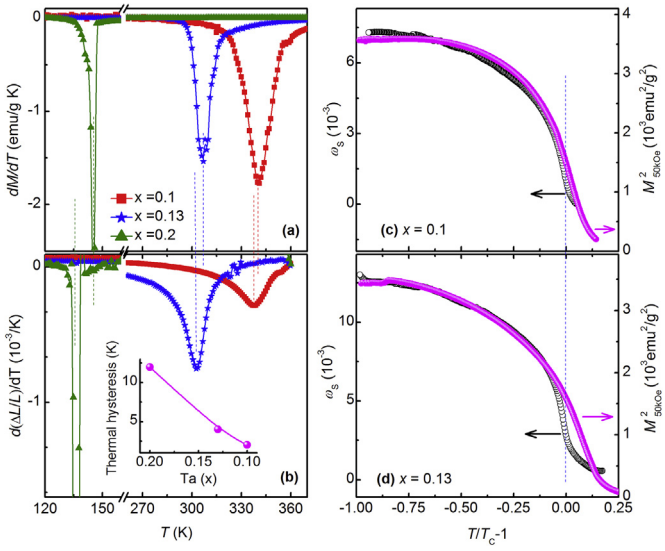

Fig. 5. (a) dM/dT recorded upon heating (b) d($\Delta L/L$)/dT measured when cooling for $x = 0.1$, 0.13 and 0.2 samples. The inset in (b) shows the thermal hysteresis for the three samples. The spontaneous volume magnetostriction (ω_S) and the square of the magnetization at 50kOe (M^2_{50kOe}) as a function reduced temperature, T/T_C-1, for $x = 0.1$ (c) and $x = 0.13$ (d). Dotted lines indicate the magnetic transitions.

magnetic transition temperatures, and can be readily ascribed to the PM signal. As the temperature is decreased, the PM resonance is slightly shifted to lower magnetic fields, suggesting an increased internal field.

As shown in Fig. 6a for $x = 0.2$, a new peak (P1) appears on the left side of the PM one at 380 K, which is strengthened upon cooling. Below 330 K, P1 is suddenly enhanced and quickly shifted to lower fields. Meanwhile, the resonance field of the PM signal starts to decrease with decreasing temperature (now this peak with reduced resonance field is named as P2). In the hexagonal crystal structure of $Hf_{1-x}Ta_xFe_2$ there are two types of Fe sites, 6h and 2a [17]. If the Fe moments in the adjacent 6h layers are antiferromagnetically coupled, the net exchange field experienced by 2a spins vanishes by symmetry because the 2a site is at the inversion center for the 6h sub-lattice [26]. As a consequence of this spin

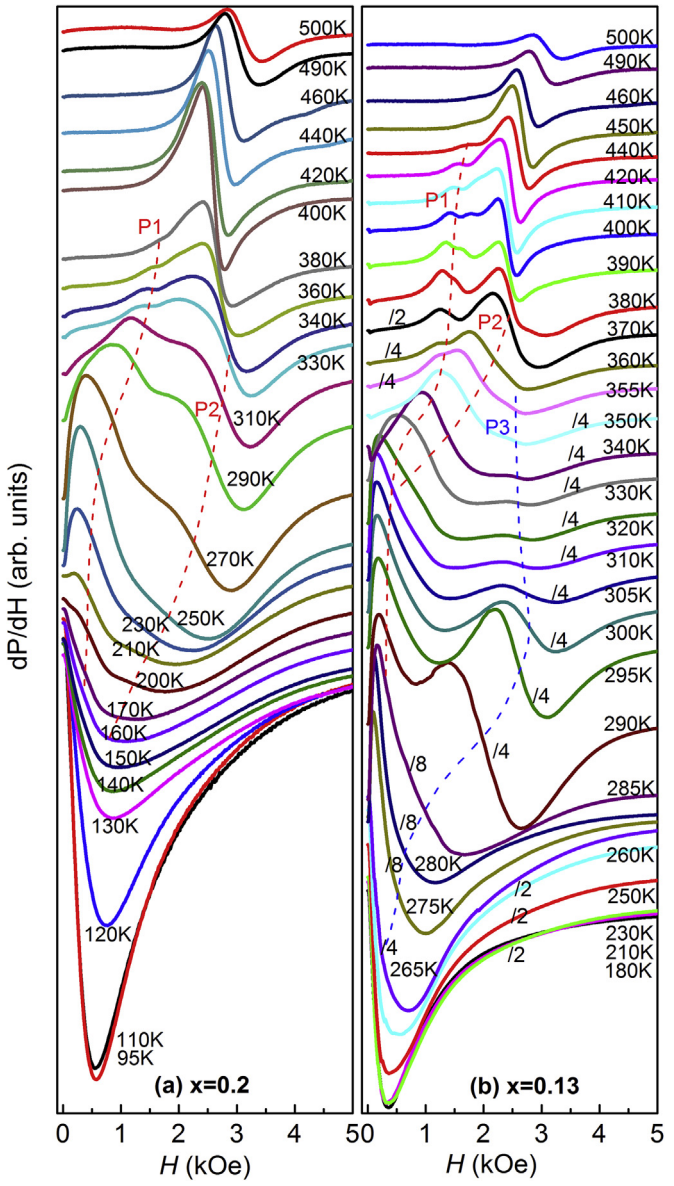

Fig. 6. ESR spectra, dP/dH, as a function of temperature for $x = 0.2$ (a) and 0.13 (b) samples. The evolutions of the different resonances are indicated by P1, P2 and P3 along with dashed lines. For clarity, the spectra are offset vertically and the spectra of $x = 0.13$ at some temperatures are divided by a constant value (either 2, or 4 or 8). The raw data can be seen in Figure S5 and S6 in the supplementary material.

frustration, the 2a Fe moments, though exist, are not ordered as revealed by Mössbauer and neutron diffraction experiments [17,26]. So both P1 and P2 are resulted from the Fe 6*h* sub-lattice.

Magnetic phase separation is normal in a frustrated magnetic system so that the overall system energy can be minimized [27]. Upon cooling, short-range FM order (P1) nucleates at some 6*h* Fe sites in PM state, which adds a local magnetic field to the non-ordered 6*h* Fe moments (P2). As a result, the resonance field of PM signal (P2) is shifted to lower field and finally overlaps with that of P1 at around $T_C \sim 140$ K. Below 270 K, both P1 and P2 are reduced in intensity with decreasing temperature, which is consistent with the fact that the AFM coupling of the Fe 6*h* sub-lattice is continuously strengthened upon cooling down to the AFM-FM transition [28]. However, the AFM order itself is usually undetectable by X-band ESR because the strong AFM spin coupling in the long-range ordered case requests a resonance field much stronger than the magnitude of 10 kOe [25]. When cooled from 140 K to 110 K, the combined single ESR peak keeps shifting to lower fields with a dramatically enhanced intensity (Figure S6 in the supplementary material). This agrees well with the sharp AFM-FM transition as observed in M(T) and $\Delta L/L$(T) curves. Below 110 K, the ESR peak is no longer changing with temperature. At this transition, the Fe moments at 2a and 6*h* sub-lattices behave synchronously since only one ESR resonance is observed, in line with the neutron diffraction and Mössbauer measurements [17,18,28].

As shown in Fig. 6b for $x = 0.13$, P1 and P2 overlap at 320 K (Figure S5 in the supplementary material). The FM ordering of Fe 6*h* sub-lattice should be completed below 315 K since the shape and intensity of this combined peak change little at lower temperatures. In $x = 0.13$ the spin frustration at 2a Fe sites is considerably released since the overall M(T) curve exhibits a FM behavior. As a result, a third ESR peak (P3) occurs at 355 K, which can be attributed to the Fe 2a sub-lattice. When cooled below 300 K, P3 starts to move to lower fields and get quickly enhanced in intensity. Finally P3 meets the combined peak due to 6*h* sub-lattice at 230 K. With further cooling, the intensity and shape of the overall ESR signal is no longer changeable, indicative of the eventual completion of FM ordering at 2a sub-lattice. The unsynchronized FM ordering processes of 2a and 6*h* Fe sub-lattices correspond to the broad PM-FM transition in $x = 0.13$.

3.4. Upgraded phase diagram

Fig. 7 shows the phase diagram of $Hf_{1-x}Ta_xFe_2$ constructed by the magnetic transition temperatures from the current study as well as from Ref. [29]. It is noticeable that $x = 0.13$ is very close to the tri-critical point in the phase diagram, where the AFM, FM and PM states converge. Here the three magnetic states are close to each other in energy [17]. Possible short-range AFM order, which is not easy to be detected by neutron diffraction and X-band ESR, may join in the FM ordering process of Fe 6*h* sites. Indeed, a magnetic field of 50 kOe is unable to satisfactorily saturate the magnetization of $x = 0.13$ at 250 K (Figure S4 in the supplementary material), which is the lower-temperature boundary of the NTE window. The surviving short-range AFM order implies the spin frustration at Fe 2a sites is not fully released in $x = 0.13$. More straightforwardly, the

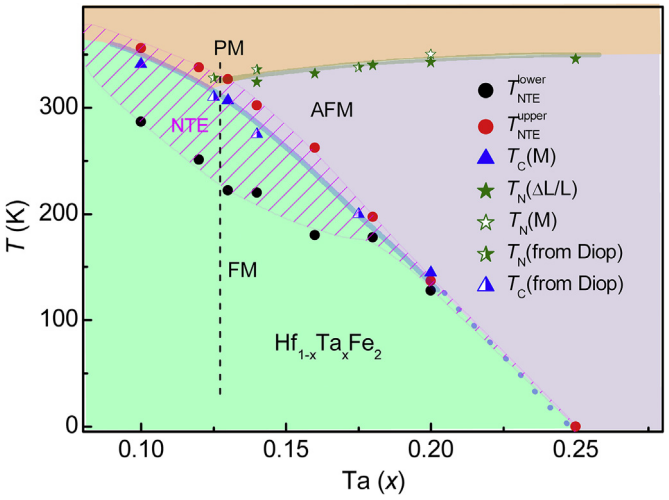

Fig. 7. Phase diagram for $Ha_{1-x}Ta_xFe_2$ ($0.1 \le x \le 0.25$). The transition temperatures (T_C, T_N) are deduced from M(T) and $\Delta L/L$(T) curves. T_C and T_N values determined by M(T) from Diop et al. are also plotted [29]. The hatched zone indicates the NTE window, determined by the upper (T_{NTE}^{upper}) and lower (T_{NTE}^{lower}) onset temperatures of NTE.

electronic coefficient of specific heat (which is a measure of spin frustrations) of $x \sim 0.13$ is obviously larger than that of $x = 0$ [30]. Due to the limited spin frustration, the ordering of Fe moments at 2a sites is still prohibited to some extent in $x = 0.13$. Only after the FM order at Fe 6*h* sites is completely established, the frustration on 2a sites can be totally removed and the long-range FM order can form at 2a sites. Unlike $x = 0.13$, the AFM and FM states are more distinguishable in energy in $x = 0.2$. In other words, the process of FM ordering at Fe 6*h* sites is free from the AFM order, which doesn't supply the frustration on Fe 2a sites. Therefore, the Fe moments at both sites enter the FM state concurrently and rapidly.

In the vicinity of FM ordering temperature, the FM resonance peak usually moves to lower fields upon cooling as a result of the enhanced magnetic moment which supplies internal fields [24,31]. The quick and concurrent shift of Fe 6*h* and 2a ESR peaks (Fig. 6a) in $x = 0.2$ thus indicates a sharp increase of the FM moment when cooled across the AFM-FM transition. For $x = 0.13$, however, the overall FM moments should grow slowly at the FM-PM transition because of the gradual and non-synchronous shifts of the Fe 2a and 6*h* ESR peaks (Fig. 6b). In the framework of SVM [23], the different growth rates of the magnetic moment indicated by the ESR data provide microscopic insights into the different sizes of NTE temperature window in $x = 0.13$ and 0.2 samples.

In a very recent report of $Hf_{1-x}Nb_xFe_2$, the broad magnetic transition and the related wide NTE temperature window were attributed to the chemical inhomogeneity [21]. However, this mechanism might not be applicable in our $Hf_{1-x}Ta_xFe_2$ samples with $0.1 \leq x \leq 0.14$ since all elements are homogeneously distributed (Fig. 1).

As x is departed from critical composition ($x \sim 0.13$) towards $x = 0$, the NTE is weakened and shifted to higher temperatures. In $Hf_{0.9-y}Zr_yTa_{0.1}Fe_2$, however, increasing Zr concentration shifts the FM-PM transition to lower temperatures, which contrasts against the effects of Ta doping on Hf sites in $Hf_{1-x}Ta_xFe_2$. Therefore, Zr doping on Hf sites draws $Hf_{0.9}Ta_{0.1}Fe_2$ back to the tricritical point. As a result, NTE properties of $Hf_{0.9}Ta_{0.1}Fe_2$ were improved upon Zr doping as displayed in Fig. 4.

3.5. Electrical and thermal transportations

Temperature dependent thermal conductivities (k) of selected samples are shown in Fig. 8a. The k values at RT of $x = 0.1$, 0.13 and 0.2 are 10.5 $W(mK)^{-1}$, 10.1 $W(mK)^{-1}$ and 9.6 $W(mK)^{-1}$, respectively. Those k values are about 20 times larger than that of commercial NTE material ZrW_2O_8, 0.5 $W(mK)^{-1}$ [13], and even as large as that of the Invar 36 alloy ($Ni_{36}Fe_{64}$), 10.4 $W(mK)^{-1}$ (Table SI, the supplementary material). Significantly, they exceed the values of the metallic NTE materials known to date, such as 6 $W(mK)^{-1}$ for $LaFe_{10.5}Co_{1.0}Si_{1.5}$ [13], 3.7 $W(mK)^{-1}$ for $Cu_{0.6}Si_{0.05}Ge_{0.35}NMn_3$ [7], and 6.4 $W(mK)^{-1}$ for $Mn_{0.98}CoGe$ [32].

As shown in Fig. 8b, the electrical conductivity (σ) decreases as the temperature rises, which is a characteristic of metals. The σ at RT is around 1.08 MS/m for $x = 0.13$. Such a high σ value resembles the value of Invar 36 alloy (1.19 MS/m, Table SI in the supplementary material), but much larger than those of other metallic NTE materials, e.g., 0.62 MS/m for $LaFe_{10.5}Co_{1.0}Si_{1.5}$ [13], 0.29 MS/m for $Cu_{0.6}Si_{0.05}Ge_{0.35}NMn_3$ [7]. The relatively high electrical and thermal conductivities suggest that $Hf_{1-x}Ta_xFe_2$ compounds are particularly useful in controlling the CTE of metals since they can largely maintain the characteristics of the matrix [33].

3.6. Mechanical properties

The basic mechanical properties, i.e., Vickers hardness, Young's modulus, and compression strength for $Hf_{1-x}Ta_xFe_2$ samples were studied. As plotted in Fig. 9a, the Vickers hardness at RT is above 850 Hv for all NTE compositions (e.g., 882 H_V for $x = 0.13$), far beyond those of most metals, Invar 36 alloy (150–200 Hv, Table SI in the supplementary material) and other NTE materials (e.g., 400 Hv for $Cu_{0.5}Ge_{0.5}NMn_3$) [4]. For Young's modulus measurement, a dynamic loading was employed and the relation between Young's modulus and penetration depth was recorded (typical curves can be seen in Figure S7, the supplementary material). The Young's modulus of each test point was then determined by averaging the values between the penetration depth of 300 nm–800 nm. As shown in Fig. 9b, the average Young's moduli of all compositions are larger than 220 GPa, which compares well with the theoretical ones for typical Laves phase compounds (e.g., 197 GPa for $TiFe_2$) [34]. The high Young's moduli well surpass the values of most metals (e.g., 117 GPa for Cu, 69 GPa for Al and 110 GPa for Ti) and Invar alloys (e.g., 141 GPa for Invar 36, Table SI in the supplementary material). $Hf_{1-x}Ta_xFe_2$ compounds also have a high compressive strength, e.g., 382 MPa for $x = 0.13$ as shown in inset of Fig. 9b. In addition to control the CTE, the good mechanical properties of the current NTE materials can be employed to strengthen the PTE matrix.

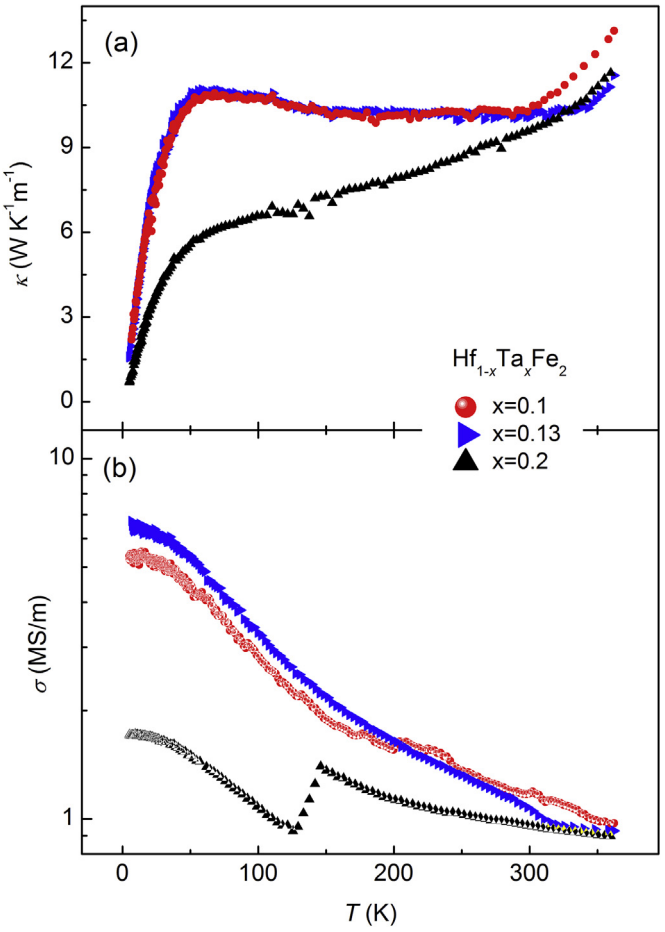

Fig. 8. Temperature dependent thermal (a) and electrical conductivities (b) of $x = 0.1$, 0.13 and $x = 0.2$ samples.

4. Conclusion

In summary, Laves phase compounds $Hf_{1-x}Ta_xFe_2$ ($0.1 \leq x \leq 0.25$) were prepared and physical properties were systematically investigated. Unlike the extensively studied compositions near $x \sim 0.2$

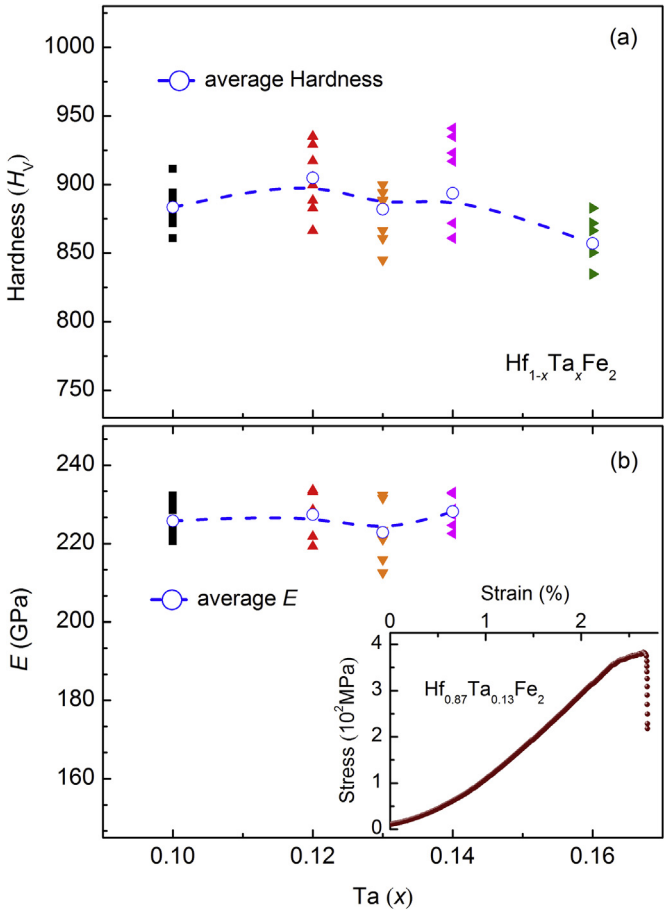

Fig. 9. (a) The x dependent Vickers hardness. (b) Young's modulus for $Hf_{1-x}Ta_xFe_2$. Open circles guided by dotted lines indicate the average values. Inset of (b) displays the compression stress-strain curve for $x = 0.13$ compound.

that shows abrupt lattice contraction at the FM-AFM transition, NTE with expanded temperature windows were observed for $0.1 \leq x \leq 0.14$. Both the NTE window ($\Delta T = 105$ K) and the magnitude of CTE ($\alpha_L = -16.3$ ppm/K) are optimized at $x = 0.13$, which is in the vicinity of the tricritical point in the phase diagram. Analysis of bulk and local magnetizations indicates the NTE is originated from SVM related with both Fe 2a and 6*h* sub-lattices. Moreover, the $Hf_{1-x}Ta_xFe_2$ compounds exhibit high thermal/electrical conductivities, Young's modulus, compressive strength and hardness. The good comprehensive performance of $Hf_{1-x}Ta_xFe_2$ compounds, which is quite rare in the reported NTE materials, is very attractive for potential application as NTE materials.

Acknowledgements

This work was supported by the Key Research Program of Frontier Sciences, CAS (QYZDB-SSW-SLH015), National Natural Science Foundation of China under contract Nos. U1632158, 51322105 and 51601189. A portion of this work was performed on the Steady High Magnetic Field Facilities, High Magnetic Field Laboratory, CAS.

Appendix A. Supplementary data

Supplementary data to this article can be found online at https://doi.org/10.1016/j.actamat.2018.09.029.

References

[1] C.P. Romao, K.J. Miller, C.A. Whitman, M.A. White, B.A. Marinkovic, Negative Thermal Expansion (Thermomiotic) Materials, Elsevier, Amsterdam, 2013.
[2] C. Lind, Two decades of negative thermal expansion Research: where do we stand? Materials 5 (2012) 1125–1154.
[3] J. Chen, L. Hu, J.X. Deng, X.R. Xing, Negative thermal expansion in functional materials: controllable thermal expansion by chemical modifications, Chem. Soc. Rev. 44 (2015) 3522–3567.
[4] Y. Nakamura, K. Takenaka, A. Kishimoto, H. Takagi, Mechanical properties of metallic perovskite $Mn_3Cu_{0.5}Ge_{0.5}N$: high-stiffness isotropic negative thermal expansion material, J. Am. Ceram. Soc. 92 (2009) 2999–3003.
[5] Q. Zhang, L.T. Jiang, G.H. Wu, Microstructure and thermo-physical properties of a SiC/pure-Al composite for electronic packaging, J. Mater. Sci. Mater. Electron. 25 (2013) 604–608.
[6] H. Reveron, L. Blanchard, Y. Vitupier, E. Riviere, G. Bonnefont, G. Fantozzi, Spark Plasma Sintering of fine alpha-silicon nitride ceramics with LAS for spatial applications, J. Eur. Ceram. Soc. 31 (2011) 645–652.
[7] R.J. Huang, Z.X. Wu, H.H. Yang, Z. Chen, X.X. Chu, L.F. Li, Mechanical and transport properties of low-temperature negative thermal expansion material Mn_3CuN co-doped with Ge and Si, Cryogenics 50 (2010) 750–753.
[8] T.A. Mary, J.S.O. Evans, T. Vogt, A.W. Sleight, Negative thermal expansion from 0.3 to 1050 Kelvin in ZrW_2O_8, Science 272 (1996) 90–92.
[9] B.K. Greve, K.L. Martin, P.L. Lee, P.J. Chupas, K.W. Chapman, A.P. Wilkinson, Pronounced negative thermal expansion from a simple structure: cubic ScF_3, J. Am. Chem. Soc. 132 (2010) 15496–15498.
[10] M. Azuma, W.-t. Chen, H. Seki, M. Czapski, S. Olga, K. Oka, M. Mizumaki, T. Watanuki, N. Ishimatsu, N. Kawamura, S. Ishiwata, M.G. Tucker, Y. Shimakawa, J.P. Attfield, Colossal negative thermal expansion in $BiNiO_3$ induced by intermetallic charge transfer, Nat. Commun. 2 (2011) 347.
[11] H. Yamamoto, T. Imai, Y. Sakai, M. Azuma, Colossal negative thermal expansion in electron-doped $PbVO_3$ perovskites, Angew Chem. Int. Ed. Engl. 57 (2018) 1–5.
[12] M. Schilfgaarde, I.A. Abrikosov, B. Johansson, Origin of the Invar effect in iron–nickel alloys, Nature 400 (1999) 46–49.
[13] R.J. Huang, Y.Y. Liu, W. Fan, J. Tan, F.R. Xiao, L.H. Qian, L.F. Li, Giant negative thermal expansion in $NaZn_{13}$-type La(Fe, Si, Co)$_{13}$ compounds, J. Am. Chem. Soc. 135 (2013) 11469–11472.
[14] Y.Y. Zhao, F.X. Hu, L.F. Bao, J. Wang, H. Wu, Q.Z. Huang, R.R. Wu, Y. Liu, F.R. Shen, H. Kuang, M. Zhang, W.L. Zuo, X.Q. Zheng, J.R. Sun, B.G. Shen, Giant negative thermal expansion in bonded MnCoGe-based compounds with Ni_2in-type hexagonal structure, J. Am. Chem. Soc. 137 (2015) 1746–1749.
[15] K. Takenaka, H. Takagi, Giant negative thermal expansion in Ge-doped anti-perovskite manganese nitrides, Appl. Phys. Lett. 87 (2005) 261902.
[16] K. Hoshi, Pressure effect on the magnetic properties of $Hf_{1-x}Ta_xFe_2$, J. Phys. Soc. Jpn. 57 (1988) 3112–3118.
[17] B. Li, X.H. Luo, H. Wang, W.J. Ren, S. Yano, C.W. Wang, J.S. Gardner, K.D. Liss, P. Miao, S.H. Lee, T. Kamiyama, R.Q. Wu, Y. Kawakita, Z.D. Zhang, Colossal negative thermal expansion induced by magnetic phase competition on frustrated lattices in Laves phase compound (Hf, Ta)Fe_2, Phys. Rev. B 93 (2016) 224405.
[18] L.V.B. Diop, O. Isnard, E. Suard, D. Benea, Neutron diffraction study of the itinerant-electron metamagnetic $Hf_{0.825}Ta_{0.175}Fe_2$ compound, Solid State Commun. 229 (2016) 16–21.
[19] Y. Muraoka, M. Shiga, Y. Nakamura, Thermal expansion of TTe_2 (T=Zr, Hf, Ti, Sc and Ce) Laves phase intermetallic compounds, J. Phys. Soc. Jpn. 40 (1976) 905–906.
[20] Y.Z. Song, J. Chen, X.Z. Liu, C.W. Wang, Q.L. Gao, Q. Li, L. Hu, J. Zhang, S.T. Zhang, X.R. Xing, Structure, magnetism, and tunable negative thermal expansion in (Hf,Nb)Fe_2 alloys, Chem. Mater. 29 (2017) 7078–7082.
[21] H. Yibole, A.K. Pathak, Y. Mudryk, F. Guillou, N. Zarkevich, S. Gupta, V. Balema, V.K. Pecharsky, Manipulating the stability of crystallographic and magnetic sub-lattices: a first-order magnetoelastic transformation in transition metal based Laves phase, Acta Mater. 154 (2018) 365–374.
[22] J.C. Lin, P. Tong, X.J. Zhou, H. Lin, Y.W. Ding, Y.X. Bai, L. Chen, X.G. Guo, C. Yang, B. Song, Y. Wu, S. Lin, W.H. Song, Y.P. Sun, Giant negative thermal expansion covering room temperature in nanocrystalline GaN_xMn_3, Appl. Phys. Lett. 107 (2015) 131902.
[23] S. Iikubo, K. Kodama, K. Takenaka, H. Takagi, S. Shamoto, Magnetovolume effect in $Mn_3Cu_{1-x}Ge_xN$ related to the magnetic structure: neutron powder diffraction measurements, Phys. Rev. B 77 (2008), 020409(R).
[24] J. Deisenhofer, D. Braak, H.A. Krug von Nidda, J. Hemberger, R. Eremina, V. Ivanshin, A. Balbashov, G. Jug, A. Loidl, T. Kimura, Y. Tokura, Observation of a griffiths phase in paramagnetic $La_{1-x}Sr_xMnO_3$, Phys. Rev. Lett. 95 (2005) 257202.
[25] J.C. Lin, P. Tong, D.P. Cui, C. Yang, J. Yang, S. Lin, B.S. Wang, W. Tong, L. Zhang, Y.M. Zou, Y.P. Sun, Unusual ferromagnetic critical behavior owing to short-range antiferromagnetic correlations in antiperovskite $Cu_{1-x}NMn_{3+x}$ ($0.1 \leq x \leq 0.4$), Sci. Rep. 5 (2015) 7933.
[26] H.R. Rechenberg, L. Morellon, P.A. Algarabel, M.R. Ibarra, Magnetic moment at highly frustrated sites of antiferromagnetic Laves phase structures, Phys. Rev. B 71 (2005) 104412.
[27] R. Ballou, Geometric frustration in the RMn_2 Laves phase compounds, Can. J. Phys. 79 (2001) 1475–1485.

[28] Y.-J. Huang, S.-Z. Li, Z.-D. Han, W.-X. Wang, Z.-Y. Jiang, S.-L. Huang, J. Lin, Y.-F. Hsia, Mossbauer study of the spin reorientation in pseudobinary alloy $Hf_{0.82}Ta_{0.18}Fe_2$, J. Alloy. Comp. 427 (2007) 37–41.
[29] L.V.B. Diop, J. Kastil, O. Isnard, Z. Arnold, J. Kamarad, Collapse of ferromagnetism in itinerant-electron system: a magnetic, transport properties, and high pressure study of $(Hf,Ta)Fe_2$ compounds, J. Appl. Phys. 116 (2014) 163907.
[30] H. Wada, N. Shimamura, M. Shiga, Thermal and transport properteis of $Hf_{1-x}Ta_xFe_2$, Phys. Rev. B 48 (1993) 10221–10226.
[31] A.I. Shames, E. Rozenberg, C. Martin, A. Maignan, B. Raveau, G. André, G. Gorodetsky, Crystallographic structure and magnetic ordering in $CaMn_{1-x}Ru_xO_3$ ($x \leq 0.40$) manganites: neutron diffraction, ac susceptibility, and electron magnetic resonance studies, Phys. Rev. B 70 (2004) 134433.
[32] F. Zhu, J.C. Lin, W.B. Jiang, C. Yang, L.F. Li, X.K. Zhang, W.H. Song, X.B. Zhu, P. Tong, Y.P. Sun, Enhanced mechanical properties and large magnetocaloric effect in epoxy-bonded $Mn_{0.98}CoGe$, Scripta Mater. 150 (2018) 96–100.
[33] E. Della Gaspera, R. Tucker, K. Star, E.H. Lan, Y.S. Ju, B. Dunn, Copper-based conductive composites with tailored thermal expansion, ACS Appl. Mater. Interfaces 5 (2013) 10966–10974.
[34] Z.-S. Nong, J.-C. Zhu, Y. Cao, X.-W. Yang, Z.-H. Lai, Y. Liu, A first-principles study on the structural, elastic and electronic properties of the C14 Laves phase compounds TiX_2 (X=Cr, Mn, Fe), Physica B 419 (2013) 11–18.